Tightly-coupled Integration of GPS/INS and Simultaneous Localisation and Mapping

Jonghyuk Kim, Jiantong Cheng[1] and Jose Guivant[2]
The Australian National University, Australia, jonghyuk.kim@anu.edu.au
[1] Key Laboratory of Complex Aviation System Simulation, Beijing, China
cheng_jiantong@163.com
[2] School of Mechanical and Manufacturing Engineering, UNSW, Australia
j.guivant@unsw.edu.au

Abstract

This paper presents a tightly integrated navigation system combining global positioning system (GPS) and inertial-based simultaneous localization and mapping (SLAM) for UAV platforms. GPS raw measurements, called pseudorange and pseudorange rate, are directly fused to an inertial SLAM filter. A compressed form of unscented filtering is implemented by partitioning the map into a local and global one. The performance of the proposed method is analysed using a high-fidelity 6-degrees-of-freedom simulator, demonstrating accurate and robust navigation even under a *single* satellite observation. The information gain of bearing and elevation angles is further analysed offering effective sensing strategies.

1 INTRODUCTION

With the advances in low-cost inertial sensor technology and global positioning system (GPS), the six-degrees-of-freedom (6-DOF) vehicle state can be effectively estimated by fusing GPS and inertial information, which has been a crucial step towards autonomous guidance and flight control [12, 10].

In many robotic applications however, the vehicles need to perform tasks close to environments, for example underground, urban canyon or forest, where GPS signal can be degraded or completely blocked. SLAM has been actively investigated to overcome this issue by mapping unknown environments, whilst simultaneously localising the vehicle utilising the on-line constructed map [3]. Contrast to conventional navigation systems, such as terrain and image matching systems, no infrastructure or *a prior* information about the environment is required, making it quite attractive for standalone or aided navigation in GPS-denied environments [11, 9, 4],

The feasibility of integrating GPS measurement and SLAM has been previously studied. [7] demonstrates a loosely-coupled integration of GPS and Inertial SLAM and [2] showed a tightly-coupled integration for a 3-DOF land vehicle model (thus non-inertial based). The work in [1] combined a compressed SLAM [5] and unscented filtering to relieve the nonlinearity in the sensing and vehicle model. In this work, we further elaborate our previous work using a full 6-DOP inertial navigation model aiming for UAV applications.

The key contributions of this paper are:

- Tightly-coupled integration of GPS and inertial SLAM using a full 6-DOP model
- Performance analysis with a varying number of satellite measurements
- Analysis of the geometrical effects of angular observation on the position solution.

The overall architecture of the fusion system is shown in Fig. 1. The measurement consists of pseudorange and pseudorange rates from visible satellite vehicles, and bearing and elevation angles from a camera. The initial positions of landmarks can be estimated by a triangulation process but in this work a range is assumed available to simplify the implementation of the method. The map database is maintained within the fusion filter by storing estimated landmark positions and orbital ephemeris of the satellite vehicles.

The remainder of the paper is outlined as follows. In Section 2, we review the unscented filtering method. We then provide the integration of GPS and IMU-based SLAM in an unscented filtering framework in Section 3, and extend it to compressed filter form in Section 4. Experimental results will be shown in Section 5 with further analysis on the geometrical effects of angular measurement in Section 6, followed by Conclusion.

2 Background on Unscented filtering

The unscented filter has been proposed for the nonlinear state estimation based on the unscented transformation, in which multivariate moment integrals can be numerically approximated [6, 1]. In contrast to the EKF, the

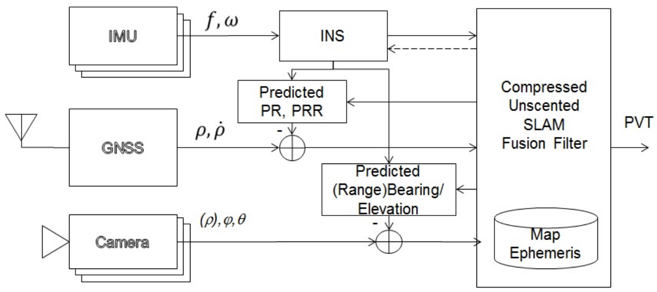

Figure 1: The system architecture for tightly-coupled GPS and inertial SLAM.

linearization and the evaluation of Jacobian matrices are not required making it a Jacobian-free method. To efficiently approximate the nonlinear transformation, a set of samples, called sigma points, are drawn along with normalized weights to capture the distribution of the state vector. Then these points are used for nonlinear transformation.

At the prediction step, first an augmented vector is formed comprising the state vector $\bar{\boldsymbol{X}}_{k|k}$ and the control input with an augmented covariance matrix $\overline{\mathbf{P}}_{k|k}$

$$\bar{\boldsymbol{X}}_{k|k} = \begin{bmatrix} \hat{\boldsymbol{X}}_{k|k} \\ \hat{\boldsymbol{U}}_k \end{bmatrix}, \quad \overline{\mathbf{P}}_{k|k} = \begin{bmatrix} \mathbf{P}_{k|k} & \mathbf{0} \\ \mathbf{0} & \mathbf{Q}_k \end{bmatrix} \tag{1}$$

Then the sigma points $\{\boldsymbol{\chi}^i_{k|k}\}_{i=0}^{2n}$ are selected from the augmented vector, with n being $dim(x) + dim(u)$, and corresponding weights w_i,

$$\begin{aligned} \boldsymbol{\chi}^0_{k|k} &= \bar{\boldsymbol{X}}_{k|k},\ \mathrm{w}_0 = \frac{\kappa}{n+\kappa} \\ \boldsymbol{\chi}^i_{k|k} &= \bar{\boldsymbol{X}}_{k|k} + \left[\sqrt{(n+\kappa)\bar{\boldsymbol{P}}_{k|k}}\right]_i,\ \mathrm{w}_i = \frac{1}{2(n+\kappa)} \\ \boldsymbol{\chi}^{i+n}_{k|k} &= \bar{\boldsymbol{X}}_{k|k} - \left[\sqrt{(n+\kappa)\bar{\boldsymbol{P}}_{k|k}}\right]_i,\ \mathrm{w}_{i+n} = \frac{1}{2(n+\kappa)} \end{aligned} \tag{2}$$

where $[\mathbf{A}]_i$ represents the i^{th} column of a matrix $\mathbf{A}$. κ is a design parameter to scale the sigma points, commonly selected so that the scale parameter $n + \kappa = 3$ for Gaussian distributions [8, 6]. The mean $\hat{\boldsymbol{X}}_{k+1|k}$ and covariance matrix $\mathbf{P}^{xx}_{k+1|k}$ of the predicted state are computed using the predicted sigma points $\boldsymbol{\chi}^i_{k+1|k} = \mathbf{f}(\boldsymbol{\chi}^i_{k|k})$,

$$\begin{aligned} \hat{\boldsymbol{X}}_{k+1|k} &= \sum_{i=0}^{2n} \mathrm{w}_i \boldsymbol{\chi}^i_{k+1|k} \\ \mathbf{P}^{xx}_{k+1|k} &= \sum_{i=0}^{2n} \mathrm{w}_i \left(\boldsymbol{\chi}^i_{k+1|k} - \boldsymbol{\chi}^0_{k+1|k}\right)\left(\boldsymbol{\chi}^i_{k+1|k} - \boldsymbol{\chi}^0_{k+1|k}\right)^T \end{aligned} \tag{3}$$

At the measurement update stage, a set of sigma points $\{\boldsymbol{\chi}^i_{k+1|k}\}_{i=0}^{2n}$ is selected from the predicted state (typically the control input is not related to measurement and thus not included in sampling) and is used to predict the sigma points $\mathcal{Z}^i_{k+1} = \mathbf{h}(\boldsymbol{\chi}^i_{k+1|k})$. The predicted measurement and related cross-correlation and covariance matrices are computed accordingly

$$\begin{aligned} \hat{\boldsymbol{Z}}_{k+1} &= \sum_{i=0}^{2n} \mathrm{w}_i \mathcal{Z}^i_{k+1} \\ \mathbf{P}_{zz,k+1} &= \sum_{i=0}^{2n} \mathrm{w}_i \left(\mathcal{Z}^i_{k+1} - \mathcal{Z}^0_{k+1}\right)\left(\mathcal{Z}^i_{k+1} - \mathcal{Z}^0_{k+1}\right)^T \\ \mathbf{P}_{xz,k+1} &= \sum_{i=0}^{2n} \mathrm{w}_i \left(\boldsymbol{\chi}^i_{k+1|k} - \boldsymbol{\chi}^0_{k+1|k}\right)\left(\mathcal{Z}^i_{k+1} - \mathcal{Z}^0_{k+1}\right)^T. \end{aligned} \tag{4}$$

Finally, the state and covariance matrix can be updated as follows

$$\begin{aligned} \mathbf{S}_{k+1} &= \mathbf{P}_{zz,k+1} + \mathbf{R}_{k+1} \\ \mathbf{K}_{k+1} &= \mathbf{P}_{xz,k+1}\mathbf{S}^{-1}_{k+1} \\ \hat{\boldsymbol{X}}_{k+1|k+1} &= \hat{\boldsymbol{X}}_{k+1|k} + \mathbf{K}_{k+1}(\boldsymbol{Z}_{k+1} - \hat{\boldsymbol{Z}}_{k+1}) \\ \mathbf{P}_{k+1|k+1} &= \mathbf{P}_{k+1|k} - \mathbf{K}_{k+1}\mathbf{S}_{k+1}\mathbf{K}^T_{k+1} \end{aligned} \tag{5}$$

If a new landmark $\boldsymbol{l}_k$ is observed, it should be initialized and augmented through a non-linear initialization function $\boldsymbol{g}(\cdot)$ which is the inverse process of the measurement function $\boldsymbol{h}(\cdot)$ with a noise $\boldsymbol{\nu}_k$,

$$\boldsymbol{l}_k = g(\boldsymbol{x}_k, \boldsymbol{z}_k, \boldsymbol{\nu}_k). \tag{6}$$

3 Unscented Inertial SLAM

The full state vector is partitioned into a local map and a global map with the estimated state vector and covariance matrix being

$$\left[\begin{array}{c} \hat{\boldsymbol{x}}_L \\ \hline \hat{\boldsymbol{x}}_G \end{array}\right] = \left[\begin{array}{c} \hat{\boldsymbol{x}} \\ \hat{\boldsymbol{m}}_L \\ \hline \hat{\boldsymbol{m}}_G \end{array}\right] \tag{7}$$

$$\left[\begin{array}{c|c} \mathbf{P}_L & \mathbf{P}_{LG} \\ \hline \mathbf{P}_{GL} & \mathbf{P}_{GG} \end{array}\right] = \left[\begin{array}{cc|c} \mathbf{P}_{xx} & \mathbf{P}_{xm} & \mathbf{P}_{LG} \\ \mathbf{P}_{mx} & \mathbf{P}_{mm} & \\ \hline \multicolumn{2}{c|}{\mathbf{P}_{GL}} & \mathbf{P}_{GG} \end{array}\right], \tag{8}$$

where the local state $\boldsymbol{x}_L$ includes the vehicle state $\boldsymbol{x}$ and the local landmarks $\boldsymbol{m}_L$, while other landmarks are stacked in $\boldsymbol{m}_G$.

The unscented filter in SLAM utilises a partial sampling scheme as the nonlinearity appears only in the vehicle state transition, whilst the map state having linear dynamics. The equivalence of partial sampling and full sampling scheme was provided in [1] showing that the performance of the partial sampled filter is not affected by the number of feature landmarks.

The state vector $\boldsymbol{x}_L$ consists of the vehicle sate (INS state and receiver clock state), the map state with the control input from IMU measurement,

$$\mathbf{x}_k = [\mathbf{p}^T, \mathbf{v}^T, \boldsymbol{\phi}^T, \mathbf{b}_a^T, \mathbf{b}_g^T, ct_b, ct_d^T]^T \tag{9}$$

$$\mathbf{m}_k = [\mathbf{m}_1^T, \mathbf{m}_2^T, \cdots, \mathbf{m}_L^T]^T \tag{10}$$

$$\mathbf{u}_k = [\mathbf{f}^T, \boldsymbol{\omega}^T]^T, \tag{11}$$

with

- Vehicle position $\mathbf{p} = [x, y, z]$[1]
- Vehicle velocity $\mathbf{v} = [v_x, v_y, v_z]$
- Euler angles $\boldsymbol{\phi} = [\phi, \theta, \psi]$
- Accelerometer bias $\mathbf{b}_a = [b_x^a, b_y^a, b_z^a]$
- Gyroscope bias $\mathbf{b}_g = [b_x^g, b_y^g, b_z^g]$
- Receiver clock bias ct_b with c being the speed of light
- Receiver clock drift ct_d
- Map position $\mathbf{m}_i = [m_{ix}, m_{iy}, m_{iz}]$
- IMU control input $\mathbf{u}_k = [\mathbf{f}, \boldsymbol{\omega}]$.

3.1 Prediction

The state transformation function can be decoupled into a nonlinear part $\hat{\boldsymbol{x}}_{k+1|k} = \mathbf{f}(\hat{\boldsymbol{x}}_{k|k})$ and a linear part $\hat{\boldsymbol{m}}_{k+1|k} = \hat{\boldsymbol{m}}_{k|k}$, thus giving

$$\left[\begin{array}{c} \hat{\boldsymbol{p}}_{k+1} \\ \hat{\boldsymbol{v}}_{k+1} \\ \hat{\boldsymbol{\psi}}_{k+1} \\ \hat{\boldsymbol{b}}_{a,k+1} \\ \hat{\boldsymbol{b}}_{g,k+1} \\ c\hat{t}_{b,k+1} \\ c\hat{t}_{d,k+1} \\ \hline \hat{\boldsymbol{m}}_{k+1} \end{array}\right] = \left[\begin{array}{c} \hat{\boldsymbol{p}}_k + \hat{\boldsymbol{v}}_k \Delta T \\ \hat{\boldsymbol{v}}_k + \boldsymbol{C}_{b,k}^n (\hat{\boldsymbol{f}}_k + \hat{\boldsymbol{b}}_{a,k}) \Delta T + \boldsymbol{g}^n \Delta T \\ \hat{\boldsymbol{\psi}}_k + \boldsymbol{E}_{b,k}^n (\hat{\boldsymbol{\omega}}_k + \hat{\boldsymbol{b}}_{g,k}) \Delta T \\ \hat{\boldsymbol{b}}_{a,k} \\ \hat{\boldsymbol{b}}_{g,k} \\ c\hat{t}_{b,k} + c\hat{t}_{b,k} \Delta T \\ c\hat{t}_{d,k} \\ \hline \hat{\boldsymbol{m}}_k \end{array}\right], \tag{12}$$

with ΔT being the prediction sampling time and $\boldsymbol{g}^n$ the gravitational vector $[0; 0; 9.8]^T (m/s^2)$.

For the control augmented vector, the sigma points $\{\boldsymbol{\chi}_{k|k}^i\}_{i=0}^{2n}$ are selected with corresponding weights w_i, where $n = dim(x) + dim(u) = 23$. The distribution of the predicted state $\boldsymbol{x}_{k+1|k}$ can then be calculated according to (3). The cross-correlation $\mathbf{P}_{xm,k+1|k}$ between $\boldsymbol{x}_{k+1|k}$ and $\boldsymbol{m}_{k+1|k}$ needs to be computed as in [1],

$$\begin{aligned} \mathbf{P}_{xm,k+1|k} &= \underbrace{\left(\sum_{i=0}^{2n_x} \mathrm{w}_i \tilde{\boldsymbol{\chi}}_{k+1|k}^i \tilde{\boldsymbol{\chi}}_{k|k}^{i,T} \mathbf{P}_{xx,k|k}^{-1} \right)}_{\mathbf{F}_{k+1}} \mathbf{P}_{xm,k|k} \\ &\triangleq \mathbf{F}_{k+1} \mathbf{P}_{xm,k|k} \end{aligned} \tag{13}$$

where $\tilde{\boldsymbol{\chi}}_{k+1|k}^i = \boldsymbol{\chi}_{k+1|k}^i - \boldsymbol{\chi}_{k+1|k}^0$ and $\mathbf{F}_{k+1}$ is equivalent to the *inferred* Jacobian as in [6].

[1]For simplicity, the transpose notation is sometimes omitted in this paper

3.2 Update

The measurement consists of either GPS pseudorange and pseudorange rate measurement from a satellite vehicle or a range/bearing/elevation measurement from a landmark

$$\boldsymbol{z}_k = \begin{cases} \boldsymbol{z}_k^i = \left[\begin{array}{cc} \rho_k^i & \dot{\rho}_k^i \end{array} \right], & \text{for } i^{th}\text{- Satellite Vehicle, or} \\ \boldsymbol{z}_k^j = \left[\begin{array}{ccc} \rho_k^j & \phi_k^j & \theta_k^j \end{array} \right], & \text{for } j^{th}\text{-Landmark} \end{cases}$$

where pseudorange $\rho_k^i = \|\boldsymbol{P}_{SV}^i - \boldsymbol{p}_k\|_2 + ct_{b,k} + v_\rho$, pseudorange rate $\dot{\rho}_k^i = \|\boldsymbol{V}_{SV}^i - \boldsymbol{v}_k\|_2 + ct_{d,k} + v_{\dot{\rho}}$ and $(\rho_k^j, \phi_k^j, \theta_k^j)$ is a range, bearing and elevation measurement.

Using the drawn sigma points, the predicted measurement and its covariance can be computed as in Equation 4. The cross-correlation between the state and measurement can be directly computed using the sigma points

$$\begin{aligned} \mathbf{P}_{xz,k+1} &= \mathbf{P}_{xx,k|k} \underbrace{\left(\sum_{i=0}^{2n_x} \mathrm{w}_i \tilde{\mathcal{Z}}_{k+1|k}^i \tilde{\mathcal{Z}}_{k|k}^{i,T} \mathbf{P}_{xx,k|k}^{-1} \right)^T}_{\mathbf{H}_{k+1}^T} \\ &\triangleq \mathbf{P}_{xx,k+1|k} \mathbf{H}_{k+1}^T \end{aligned} \tag{14}$$

where $\tilde{\mathcal{Z}}_{k+1|k}^i = \mathcal{Z}_{k+1|k}^i - \mathcal{Z}_{k+1|k}^0$ and $\mathbf{H}_{k+1}$ is an *inferred* measurement Jacobian from the sigma samples.

3.3 Initialisation

The sigma points $\boldsymbol{\chi}_{k|k}^i\}$ are used to predict the landmark position $\{\mathcal{L}_{k|k}^i\}$ and the cross-correlations with the vehicle and map are computed respectively as

$$\begin{aligned} \mathbf{P}_{xl,k|k} &= \underbrace{\left(\sum_{i=0}^{2n_x} \mathrm{w}_i \tilde{\mathcal{L}}_{k|k}^i \tilde{\mathcal{L}}_{k|k}^{i,T} \mathbf{P}_{xx,k|k}^{-1} \right)}_{\mathbf{G}_k} \mathbf{P}_{xx,k|k} \\ &= \mathbf{G}_k \mathbf{P}_{xx,k|k} \end{aligned} \tag{15}$$

$$\mathbf{P}_{ml,k|k} = \mathbf{G}_k \mathbf{P}_{xm,k|k} \tag{16}$$

where $\mathcal{L}_{k|k}^i = \mathcal{L}_{k|k}^i - \mathcal{L}_{k|k}^{i+n_{xz}}$.

4 Compressed Implementation

In the local area, we can efficiently predict $\hat{\boldsymbol{x}}_{L,k+1|k}$ and $\mathbf{P}_{L,k+1|k}$ in real-time using the local *inferred* Jacobian (termed a local linear factor) $\mathbf{F}_{k+1}$ for the propagation of $\mathbf{P}_{xm,k|k}$ as in (13). Correspondingly, the global linear factor $\mathbf{F}_{G,k+1}$ for the prediction of $\mathbf{P}_{LG,k+1|k}$ can be extended as

$$\mathbf{F}_{G,k+1} = \left[\begin{array}{cc} \mathbf{F}_{k+1} & \mathbf{0} \\ \mathbf{0} & \mathbf{I}_{n_G} \end{array} \right]. \tag{17}$$

For the j^{th} landmark observation, we can get a local linear factor $\mathbf{H}_{k+1} = [\mathbf{H}_{x,k+1}, \mathbf{H}_{m,k+1}]$ as to (14), where $\mathbf{H}_{x,k+1}$ and $\mathbf{H}_{m,k+1}$ correspond to the vehicle state and

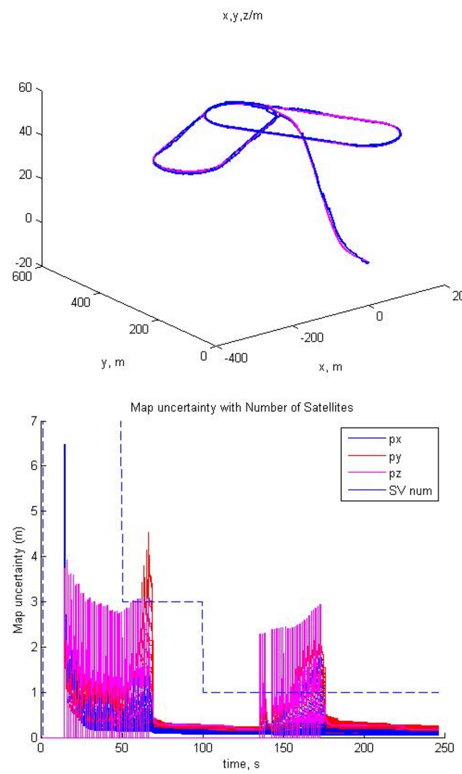

Figure 2: The evolutions of the map uncertainties along with the number of satellite vehicles which drops from 7 to 3 and 1.

the j^{th}-landmark, respectively. The global linear factor $\mathbf{H}_{G,k+1}$ for the whole map can then be computed as

$$\mathbf{H}_{G,k+1} = [\mathbf{H}_{x,k+1}, \mathbf{0}, \cdots, \mathbf{0}, \mathbf{H}_{m_j,k+1}, \mathbf{0}, \cdots, \mathbf{0}]. \quad (18)$$

Similarly, for the landmark initialization step, we can get the local linear factor $\mathbf{G}_{k+1}$ through (15), and the global linear factor $\mathbf{G}_{G,k+1}$ becomes

$$\mathbf{G}_{G,k+1} = \begin{bmatrix} \mathbf{G}_{k+1} & \mathbf{0}_{n_G} \end{bmatrix} \quad (19)$$

As described in [5], when the vehicle runs in the local area, the local prediction and update information of $\mathbf{P}_{LG}$, $\mathbf{P}_{GG}$ and $\boldsymbol{m}_G$ are preserved in three auxiliary variables, namely $\boldsymbol{\alpha}$, $\boldsymbol{\beta}$ and $\boldsymbol{\gamma}$ [2]. By using the foregoing linear factors, the full map update can be performed.

5 Experimental Results

Using a high-fidelity simulator *GPSoft*, GPS raw measurements are generated with the pseudorange noise having a standard deviation of $2m$ and pseudorange rate error with $1m/s$. The output rate of both measurements is $1Hz$. The IMU output is $100Hz$ with accelerometer bias of $2.0 \times 10^{-2} m/s^2$ and gyroscope bias of $100°/hr$ (or $2.8°/sec$). This noise levels correspond to typical low-quality and low-cost inertial sensors. For the landmark observation, 400 landmarks are simulated with a $10Hz$ output rate and a $\pm 20°$ down-looking field of view. To verify the benefits of tightly-coupled integration, the number of satellite vehicles reduces from seven to three (at $50sec$) to one (at $100sec$) which is shown as a dashed line in Fig. 2.

Figure 2(top) shows the estimated $3D$ trajectory and Fig. 2(bottom) depicts the evolution of the map uncertainties plotted with the number of satellite vehicles on the same y-axis. It can be observed that when the number of SVs dropped from seven to three, the newly initialized landmarks show larger errors due to reduced information from the SVs. The second group of large landmark uncertainties from around $140sec$ are related to the second circuit of the trajectory. It can be seen however, that those uncertainties from the two circuits approach to a similar lower bound which is determined by the sensing uncertainties. Figure 4 depicts the estimated biases from the accelerometers and gyroscopes, showing that the estimated biases converge reliably to the true biases. The convergence of the receiver clock bias and drift is also shown in Fig. 4. Due to the constant drift term, the clock bias changes linearly. It can be seen that SLAM observation can reliably and effectively estimate the receiver clock errors when the number of satellite vehicle is only one after $100sec$, which is crucial for precise ranging and timing outputs from the integrated system.

6 Geometrical Effects of Bearing/Elevation Measurements

Understanding the effects of the sensing geometry of satellite vehicles and ground landmarks can help selecting a most informative set of satellite/landmarks. One of key questions can be: given a generated SLAM map, what sensing geometry of bearing and elevation observations can maximise the information gain on the position solution?

For the purpose of analysis, we consider a simple case as illustrated in Fig.5, in which a vehicle flies a straight-line trajectory with a constant height, observing two landmarks on the ground. The information gain from the sensing is $\boldsymbol{I} \triangleq \boldsymbol{H}^T\boldsymbol{H}$ using a linearised observation matrix $\boldsymbol{H}$. If $\boldsymbol{H}$ is an invertible 3×3 matrix, then $\det(\boldsymbol{H}^T\boldsymbol{H}) = (\det(\boldsymbol{H}))^2$. Thus we investigate $\det(\boldsymbol{H})$ to gain intuitive understanding. Given the vehicle position $\boldsymbol{x} = [x, y, z]^T$ and i^{th}-landmark position $[x_i, y_i, z_i]^T$,

[2] In the original paper, $\boldsymbol{\phi}$, $\boldsymbol{\psi}$ and $\boldsymbol{\theta}$ were used as auxiliary variables. To avoid confusion with the Euler angles, $\boldsymbol{\alpha}$, $\boldsymbol{\beta}$ and $\boldsymbol{\gamma}$ are used instead. Please refer to [5] for more detailed information.

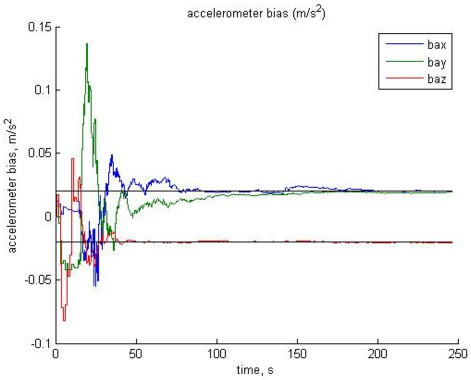

(a) Accelerometer Biases

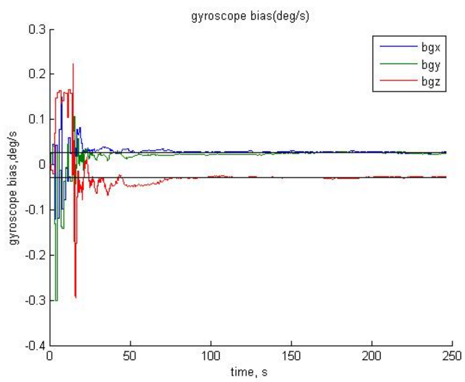

(b) Gyroscope Biases

Figure 3: The estimated IMU biases. (a) accelerometer and (b) gyroscope, with black solid lines being the true values.

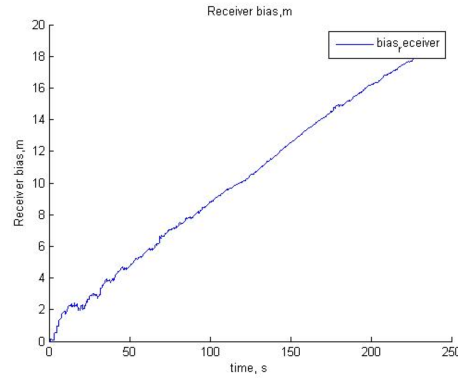

(a) Clock Bias

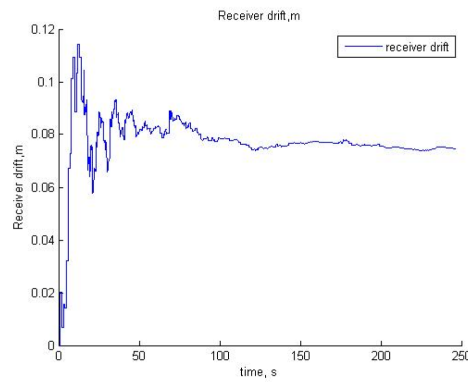

(b) Clock Drift

Figure 4: The estimated GPS receiver (a) clock bias and (b) drift. Note the linear bias due to the presence of constant drift.

the bearing ϕ_i and elevation θ_i observations are

$$\phi_i = \arctan \frac{(y_i - y)}{(x_i - x)} \tag{20}$$

$$\theta_i = \arctan \frac{(z_i - z)}{\sqrt{(x_i - x)^2 + (y_i - y)^2}}. \tag{21}$$

It can be seen that 3 observations are required to solve for 3 unknowns: x, y and z position. Thus we stack 3 angle observations $\boldsymbol{z} = [\phi_1, \phi_2, \theta_1]^T$ and by linearisation and trigonometric manipulation, the absolute value of the determinant $\det(\boldsymbol{H})$ can be shown as

$$|\det(\boldsymbol{H})| = \underbrace{\left(\frac{|\sin(\Delta\phi_{12})|}{r_{1o} r_{2o}}\right)}_{x-y} \underbrace{\left(\frac{|\cos(\theta_1)|}{r_1}\right)}_{z}, \tag{22}$$

where $\Delta\phi_{12}$ is the relative bearing angle between two landmarks, with r_{1o}, r_{2o} being the horizontal distance to each landmark, and r_1 the full range to the landmark 1. It can be observed that

- The relative bearing angle contributes to the horizontal information gain, while the elevation to the vertical information.
- When $\Delta\phi_{12} = \pm 90°$ the sine term becomes maximum and as the vehicle moves closer to the landmarks, the horizontal gain increases. If the vehicle position is along the line connecting two landmarks, the horizontal position becomes unobservable which corresponds to the condition of $\Delta\phi_{12} = 0°$ or $180°$.
- The vertical gain proportional to the cosine of the elevation and inverse range to the landmark. The maximum gain can be achieved with $\pm 45°$ elevation condition. This is illustrated in Figure 6, in which the height is set to $50m$ and a landmark is located at $[50, 0]m$. Note the vertical gain drops to zero as the vehicle flies directly over the landmark, which corresponds to the $90^{c}irc$ elevation angle and the vertical position becomes unobservable. As the vehicle moves away from the landmark, the vertical gain approaches to zero, which is related to a lower elevation angle.

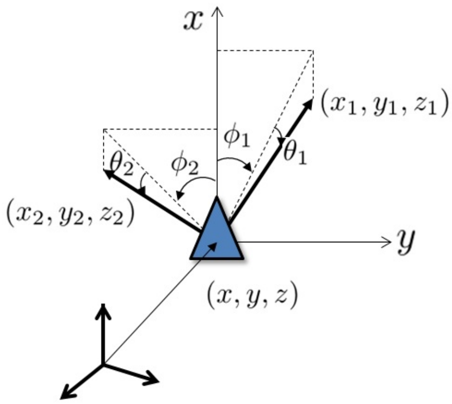

Figure 5: The sensing geometry of bearing/elevation observation from two landmarks used for analysis.

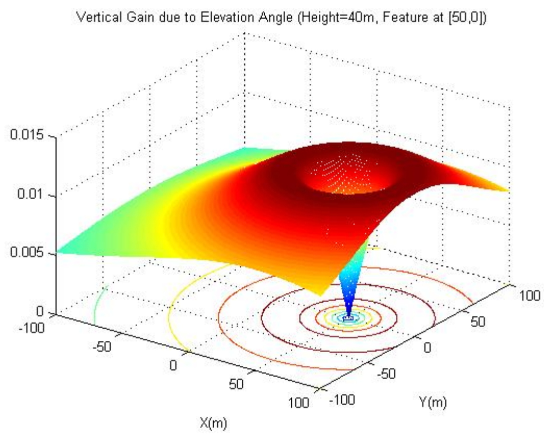

Figure 6: The vertical information gain from an elevation angle. A ground feature is simulated at $[\pm 50, 0]m$. It can be seen that the maximum gain can be achieved with a $\pm 45^circ$ elevation condition which corresponds to the top of crater.

7 Conclusions

In this paper, we presented a tightly-coupled integration of GPS and inertial-based SLAM using a full 6-DOP inertial navigation model, extending the previous work on a 3-DOP model. The simulation results demonstrated the benefits of fusing GPS pseudorange and pseudorange rates with inertial SLAM, enabling a reliable and robust navigation solution even with a *single* satellite vehicle, and the fast convergence of IMU and receiver biases. In addition, the effects of sensing geometry of bearing and elevation were analysed, showing that $\pm 90°$ relative bearing of two landmarks can maximise the horizontal information gain, whilst $\pm 45°$ elevation angle can maximise the vertical gain. Currently real flight data is being examined to verify the performance in a real environment.

References

[1] J. Cheng, J. Kim, Jiang Z., and X. Yang. Compressed unscented kalman filter-based slam. In *IEEE Conference on Robotics and Bio-mimetic*, pages 1602 – 1607, Bali, Dec. 2014.

[2] Kim J. Jiang Z. Zhang W. Cheng, J. Tightly coupled slam/gnss for land vehicle navigation. 305:721–733, 2014.

[3] Hugh Durrant-Whyte and Tim Bailey. Simultaneous localization and mapping: part i. *IEEE Robotics and Automation Magazine*, 13(2):99–110, 2006.

[4] Nathaniel Fairfield, George Kantor, and David Wettergreen. Real-time slam with octree evidence grids for exploration in underwater tunnels. *Journal of Field Robotics*, 24(12):03–21, Jan. 2007.

[5] Jose E Guivant and Eduardo Mario Nebot. Optimization of the simultaneous localization and mapbuilding algorithm for real-time implementation. *IEEE Transactions on Robotics and Automation*, 17(3):242–257, Jun. 2001.

[6] Guoquan P Huang, Anastasios I Mourikis, and Stergios I Roumeliotis. A quadratic-complexity observability-constrained unscented kalman filter for slam. *IEEE Transactions on Robotics*, 29(5):1226 – 1243, 2013.

[7] Kim J. and Sukkarieh S. 6dof slam aided gnss/ins navigation in gps denied and unknown environments. 4(1-2):120–128, Dec. 2005.

[8] Simon J Julier and Jeffrey K Uhlmann. Unscented filtering and nonlinear estimation. *Proceedings of the IEEE*, 92(3):401–422, 2004.

[9] Jonghyuk Kim and Salah Sukkarieh. Real-time implementation of airborne inertial-slam. *Robotics and Autonomous Systems*, 55(1):62–71, Jan. 2007.

[10] J. Kim, S. Sukkarieh, and S. Wishart. Real-time navigation, guidance and control of a uav using low-cost sensors. In *International Conference of Field and Service Robotics*, pages 95–100, Yamanashi, Japan, 2003.

[11] P Newman, J Leonard, Juan D Tardos, and Jos Neira. Explore and return: Experimental validation of real-time concurrent mapping and localization. In *Proc. IEEE International Conference on Robotics and Automation (ICRA)*, volume 2, pages 1802–1809, Washington, DC, May 2002.

[12] B. Parkinson. Origins, evolution, and future of satellite navigation. *Journal of Guidance, Control, and Dynamics*, 20(1):11–25, 1997.